IOP Publishing Journal Title
Journal **XX** (XXXX) XXXXXX https://doi.org/XXXX/XXXX

Low-Noise Anisotropic Magnetoresistance Sensing at 310 K: Unveiling the Optimal Doping Window in $La_{1-x}Sr_xMnO_3$ Films

Raul Solis Leon[1,2,3], Ines Garcia Manuz[2,3], Sandeep Kumar Chaluvadi[4], Victor Pierron[1], Vincent Polewczyk[4], Aleksandr Yu Petrov[4], Giovanni Vinai[4], Alain Pautrat[5], Fernando Ajejas[3], Bruno Guillet[1], Stéphane Flament[1], Pasquale Orgiani[4], Paolo Perna[3,*], Laurence Mechin[1,*]

[1] Université Caen Normandie, ENSICAEN, CNRS, Normandie Univ., GREYC UMR6072, F,14050 Caen CEDEX, France
[2] Departamento de Física de la Materia Condensada & Condensed Matter Physics Center (IFIMAC), Universidad Autónoma de Madrid, Campus de Cantoblanco, Madrid 28049, Spain
[3] IMDEA Nanoscience, C/ Faraday 9, Campus de Cantoblanco, Madrid 28049, Spain
[4] CNR - Istituto Officina dei Materiali (IOM), S.S. 14 km 163.5, I-34149, Trieste, Italy
[5] Université Caen Normandie, ENSICAEN, CNRS, Normandie Univ., CRISMAT UMR6508, 14050 Caen CEDEX, France

E-mail: paolo.perna@imdea.org ; laurence.mechin@ensicaen.fr

Received xxxxxx
Accepted for publication xxxxxx
Published xxxxxx

Abstract

Low-field AMR sensors based on epitaxial $La_{1-x}Sr_xMnO_3$ (LSMO) thin films combine ultra-low noise, high detectivity, and straightforward fabrication, offering a compelling alternative to giant and tunnel magnetoresistance technologies. By tuning Sr doping (x = 0.15-0.45) on 4° miscut $SrTiO_3$ substrates, we achieve fine control of performance parameters tailored to biomedical environments operating at tightly regulated temperatures. Shape-induced uniaxial magnetic anisotropy and Wheatstone bridge structures suppress noise and isolate the AMR signal. Temperature-dependent characterization reveals that devices with x = 0.35 deliver optimal sensitivity and lowest electronic noise at 310 K (body temperature), highlighting their strong potential for biomedical sensing applications.

Keywords: manganites, doping, anisotropic magnetoresistance, spin-orbit coupling, electronic noise

1. Introduction

Magnetic sensing techniques rely on various effects, such as magnetic flux variation, Hall effect, and magnetoresistance (MR) [1]. Among them, magnetoresistive sensors stand out for their high sensitivity and small size. While giant (GMR) and tunnel (TMR) MR sensors dominate the market [2], anisotropic MR (AMR) sensors are gaining renewed attention due to their good sensitivity and simple fabrication process [3],[4]. Unlike GMR and TMR devices, which have complex multilayer structures, AMR sensors consist of a single thin ferromagnetic (FM) layer, where resistance depends on the angle between the charge current and the magnetization vectors [5],[6].

Among ferromagnets exhibiting large AMR effect at or around room temperature, the half-metallic hole-doped manganite $La_{1-x}Sr_xMnO_3$ (LSMO) with x = 1/3 presents high magnetic sensitivity (0.1-0.3 %/mT) and low-frequency detectivity down to nT/√Hz, making it suitable for ultra-low

magnetic field sensors at human body temperature (i.e., 310 K) [7],[8].

Besides, the very rich phase diagram of LSMO allows the opportunity to finely tune its magnetic and transport properties and operation temperature by varying a little the composition (doping) and crystal structure (strain) [9]. Such a complex and rich phase diagram is due to the strong interplay between lattice, charge, and spin degree of freedom properties in all manganite compounds. In LSMO by slightly varying the dopant cation concentration in the range $0.15 < x < 0.5$, T_C can vary from 250 to 350 K. The origin of such behaviour is associated with the double exchange (DE) mechanism [10], that is the electronic conduction mechanism between two Mn ions with mixed valence states (+3 and +4) indirectly coupled via an O^{2-}. The alignment of the Mn *3d* electron spins increases the electrical conductivity, which depends directly on the doping and inversely on T/T_C and the lattice parameter. The latter may be controlled by exploiting the strain imposed by a substrate in the case of epitaxial thin films [11],[12]. Thus, by modifying Sr doping and strain we can tailor the magnetic anisotropy of the system, and consequently the magnetization reversal pathways and the MR response.

For sensing applications, a linear variation of the MR output with the applied field is desirable. To accomplish such a linear response with the magnetic field, we can use a material with a single preferential direction (easy axis, e.a.) for magnetization alignment, i.e. uniaxial anisotropy, and applying the magnetic field along the hard axis (h.a.) direction [16]. To achieve a defined uniaxial magnetic anisotropy we can resort to the substrate-induced strain and shape imposed by vicinal surfaces for the epitaxial growth of LSMO [13]. In previous works we have demonstrated the ability to tune (i.e., maximize) the AMR in $La_{2/3}Sr_{1/3}MnO_3$ by controlling the magnetic anisotropy achieved through the engineering of the thin film epitaxial growth on vicinal single crystal surfaces [14],[15],[16].

This study examines Sr doping (x) in LSMO to optimize sensor sensitivity, detectivity, and electronic noise at human body temperature. It explores the spin-orbit coupling (SOC) dependence of magnetic anisotropy, magnetization reversal, magnetoresistance, and Curie temperature (T_C) in epitaxial films deposited on vicinal substrates.

2. Results and Discussion

We have analysed LSMO thin films (120 u.c., 45 nm) grown on $SrTiO_3$ (STO) (001) with a 4º miscut angle towards the [010] crystallographic direction. Films were deposited via Reflection High-Energy Electron Diffraction (RHEED)-assisted MBE at 993 K under $2{\cdot}10^{-6}$ mbar ozone pressure, with Sr content ranging from x = 0.15 to 0.45. X-ray diffraction (XRD) analysis confirms full tensile strain, aligning the film's in-plane lattice constant with the substrate. We earlier demonstrated that, while preserving the peculiar surface morphology with defined terraces along [100] crystallographic direction, increasing x induces higher tensile strain, leading to a linear decrease in the out-of-plane lattice parameter [17], and hence intensified Jahn-Teller (JT) distortion.

The dependence of T_C and magnetization reversal pathways with the Sr-doping is presented below. In Figure 1a, we show the magnetization vs. T curves measured by SQUID at 50 mT heating the samples after field cooling under 3 T, which allow to extract the values of T_C for each composition (obtained by fitting the linear drop of the magnetization across the metal-to-insulator transition) in Figure 1b. From this, we clearly see that the samples with $x > 0.20$ present $T_C > 310$ K, that is the desired operation temperature of the sensors (human body temperature).

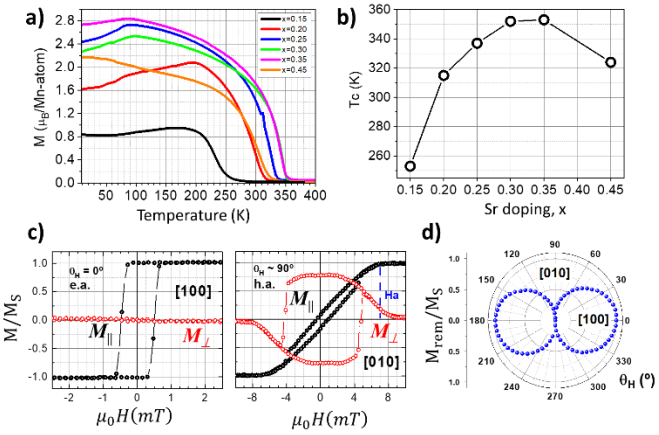

Figure 1. *Magnetic properties of 45 nm thick LSMO films with 0.15 < x < 0.45. a) Magnetization vs. temperature measured by SQUID at 50 mT during warming after it was cooled in a magnetic field of 3 T, and b) corresponding T_C vs. x. c) Magnetic field loops of the magnetization components parallel ($M_{\parallel}$) and perpendicular ($M_{\perp}$) normalized to the saturation state (M_S) to the applied field ($\mu_0 H$) at easy and hard axis of LSMO with x=0.25 at 295K. d) Corresponding angular evolution of the remanence magnetization normalized to the saturation state as function of $\theta_H = (\widehat{H, K_u})$, with K_u being the direction of the e.a. Detailed description of the set-up geometry and characterization of the other doping concentrations are reported in Supp. Info.*

The magnetic anisotropy symmetry of the samples were studied by resorting to vectorial-magneto-optical Kerr effect magnetometry (v-MOKE) [18]. In their respective FM phase, all samples present well-defined uniaxial anisotropy (see Section A1 of Supp. Info.). In Figure 1c we report on the magnetization hysteresis cycles of the representative x = 0.25 film measured at 295 K with the magnetic field applied along the direction parallel and perpendicular to the surface terraces direction, i.e. [100] and [010] respectively. Black (red) points refer to the magnetization component parallel $M_{\parallel}$ (transversal, $M_{\perp}$) to the field [13]. Through the analysis of both magnetization components, we can precisely study the magnetization reversal pathways and magnetic anisotropy symmetry in the whole angular range. We can observe square

and abrupt transitions of $M_{\parallel}$ along the easy [100] direction, indicating a magnetization reversal dominated by nucleation and propagation of magnetic domains. In contrast, along the [010] h.a. direction, an almost fully reversible variation of $M_{\parallel}$ is observed. This is typical of a magnetization reversal dominated by coherent rotation of magnetic domains [15], as also corroborated by the reversal of $M_{\perp}$. The remanence magnetization (M_{rem}) extracted from the cycles at any field direction, presents the typical two-fold symmetry that indicates a defined two-fold uniaxial symmetry of the magnetic anisotropy (Figure 1d).

In LSMO, magnetism is strictly linked to the crystal lattice, making it indispensable to study the SOC properties. To do so, we have analysed X-ray absorption spectroscopy (XAS) data acquired at the Mn $L_{2,3}$ edges with a grazing angle of 45° with respect to the X-ray beam and X-ray magnetic circular dichroism (XMCD) measurements taken in circular polarization with 75% degree of polarization and 45° of angle incidence. Measurements were taken at magnetic remanence after the application of an in-plane magnetic pulse of ±30 mT (large enough to saturate the magnetization of the samples) at each energy step along the magnetic easy axis.

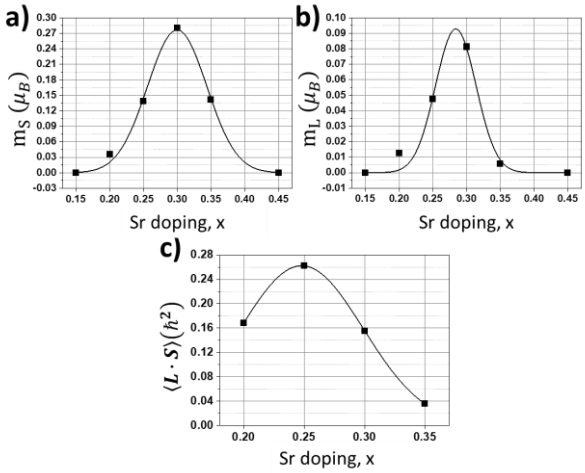

Figure 2. *Magnetic moments and strength of the SOC interaction of 45 nm thick LSMO films with 0.15 < x < 0.45, extracted from XAS-XMCD curves at 300 K. a) m_S vs. x, displaying a gaussian shape centered at x = 0.30. b) m_L vs. x, centered at x = 0.28. d) Strength of the SOC interaction $\langle \boldsymbol{L}\cdot\boldsymbol{S}\rangle (h^2)$ vs. x extracted from the heights of the L_2 and L_3 peaks of the XAS spectra also centered at x = 0.25.*

By applying the sum rules to the XAS-XMCD curves [19],[20] for different x, we obtain the spin (m_S) and orbital (m_L) magnetic moments shown in Figure 2 (the spectra and the corresponding analysis is reported in A2 of Supp. Info.). In Figure 2a, we observe that m_S vs. x presents a Gaussian behavior centered at x = 0.30, as expected for optimal FM ordering [21]. In a similar way, m_L vs. x also presents a Gaussian shape but centred at lower concentration. This is due to the effect of JT distortion that modifies the orbital overlap [11]. Finally, in Figure 2c the resulting SOC expectation value $\langle \boldsymbol{L}\cdot\boldsymbol{S}\rangle$[22],[23] centred at x = 0.25.

The AMR sensors were fabricated in Wheatstone Bridge (WB) geometry by a microlithography process, as sketched in Figure 3a (details in A3 of Supp. Info.), in order to avoid common mode noise and to remove the isotropic contribution from CMR [16]. The device consists of four resistance elements allocated in a loop, creating two branches connected in parallel, as seen in the sketch in Figure 3a. A bias voltage (V_{bias}) is applied in two opposite nodes, while output signal (V_{out}) is measured in the other two. Since the resistances of the four arms at zero magnetic field (R_0) are equal (balanced WB), $V_{out} = V_{bias} \times \frac{\Delta R}{R_0}$ with $\Delta R = R(H) - R_0$ being the variation of R with applied field. In this configuration, the angle between the injected current into the device and the magnetization varies with opposite signs for adjacent arms. To guarantee that the magnetization in all arms of the WB rotates in the same direction, there must be a slight tilt with respect to the h.a.

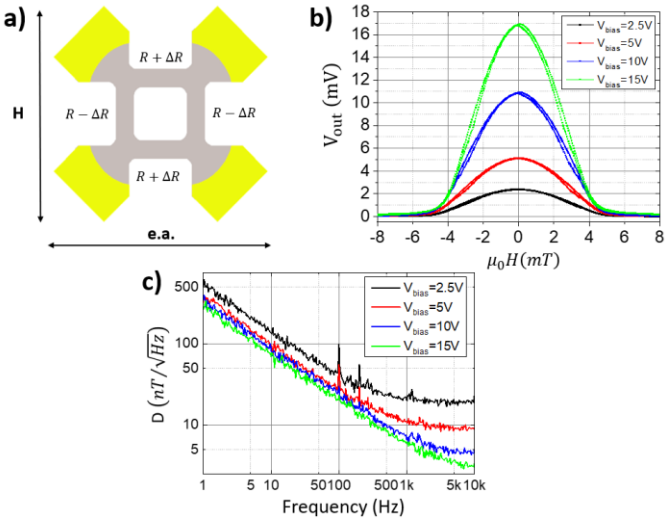

Figure 3. *Magnetoresistive and electrical noise properties of the devices. a) Sketch of the WB structure of the device, in which the direction of the applied magnetic field (along h. a.) is indicated. The resistance values for a balanced WB (positive and negative variations of the resistance for consecutive branches) are also indicated. b) Variation of the output voltage of the WB, before amplification, for different applied voltages for x = 0.25 at T = 310 K. The amplitude and sensitivity increase linearly with the applied voltage. c) Detectivity curves for x = 0.25 at T = 310 K, representing the minimum detectable signal for each frequency and applied voltage.*

Figure 3b displays the output voltage V_{out} of a WB patterned on the x = 0.25 film at 310 K for different bias voltage values, i.e., the voltage difference at the WB level before it is fed into the amplifier (the measurements corresponding to the other compositions are reported in A4,5 of Supp. Info.). At large magnetic field applied along the h.a., the sample magnetization is aligned to the external field (saturation state), and since the current direction is fixed, the MR output is minimum. Decreasing the field to zero, since the magnetization reversal is purely rotative (coherent rotation of

the magnetic domains) and being fixed the current direction, V_{out} varies gradually. When the applied field is zero, the magnetization aligns towards the magnetization easy direction, thus the AMR displays the maximum value [13],[16]. The mechanism is similar for magnetic field applied in the opposite direction.

From the experimental MR curve, we calculated the sensitivity for each bias voltage as the slope of the linear part at half the maximum: $S\left(\frac{V}{T}\right) = \frac{\partial V_{meas}}{\mu_0 \partial H} = \frac{\Delta R}{R_0}\frac{V_{bias}}{\mu_0 H_a}$, with H_a being the anisotropy field. S is thus proportional to V_{bias} and depends inversely on H_a. The latter thus needs to be reduced to have good sensitivity.

To detect weak signals, we either need to increase the signal intensity or lower the noise (i.e., random fluctuations of the signal). There are different contributions to noise (described by the power spectral density, S_v), such as thermally excited vibrations of charge carriers in conductors (Johnson-Nyquist or thermal noise, $4k_BTR_0$) and low-frequency ($1/f$) noise, which dominate at low frequencies. The $1/f$ noise in LSMO films can be described via Hooge's [25] empirical relation $\frac{S_v}{V^2} = \frac{\alpha_H}{N f^\gamma}$ where $\gamma \approx 1$, α_H is the Hooge parameter, and N the charge carrier. Other contributions arise from the electronics as the amplifiers, which introduce two sources of noise, e_{nA} the voltage noise spectral density and i_{nA} the current noise spectral density. While sensitivity refers to how well the sensor will react to a variation of the targeted physical quantity, the detectivity ($D\ [T/\sqrt{Hz}]$), which is defined as the ratio of the spectral noise density over the sensitivity, i.e., inverse to the signal to noise ratio. For high V_{bias}, $D = \frac{R_0}{\Delta R}\mu_0 H_a \sqrt{\frac{\alpha_H}{n}\frac{1}{4\Omega f}}$ and instructs about the minimum detectable signal for a given frequency, where α_H/n, the normalized Hooge parameter over number of carriers, is hence obtained from the slope of the linear region of the spectral noise density curves (see A4 of Supp. Info.), and Ω is the volume of one arm of the Wheatstone bridge. Note that D is independent from V_{bias} in the low-frequency region.

In the following we present the noise experimental results performed at 310 K and at selected temperature in the vicinity of T_C accordingly to the specific doping. Figure 3c shows the detectivity of a WB patterned in the x = 0.25 LSMO film at 310 K for different V_{bias}. At low frequencies, the curves almost overlap, and above 5 kHz, the thermal noise contribution is the only remaining term for the sensor's noise.

Figure 4a displays the sensitivity for different V_{bias} at 310 K for x = 0.25, 0.30 and 0.35 (i.e., for samples displaying FM at 310 K), which increases linearly with V_{bias}. Similarly, the variation of the sensitivity at V_{bias} = 10 V for all the concentrations and temperatures is presented in Figure4b, showing that the sensitivity is generally better for x = 0.25. Figure 4c shows clearly a significant decrease of α_H/n when doping is increased, which, at T = 310 K is almost five times between the highest (x = 0.35) and lowest (x = 0.25) doping.

Panel d shows the temperature evolution of the signal amplitude, i.e. the height of the maxima in the voltage output for V_{bias} = 10 V normalized by V_{bias}. It is seen that it decreases as increasing T up to T_C. While the amplitude of the output signal decreases with T, the slope of the curve increases, as expected due to the proximity to ferromagnetic-paramagnetic transition, indicating that the best composition for our application is x = 0.35 at $T = 310\ K$.

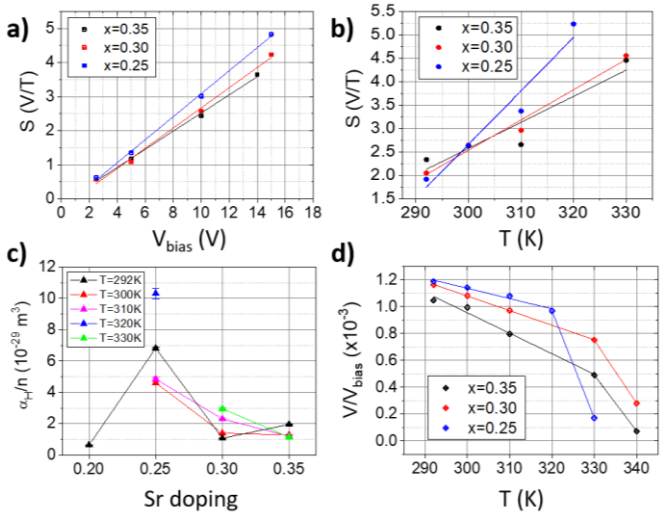

Figure 4. *a) Variation of the sensitivity for each concentration and applied voltage at T=310K. b) Behavior of the sensitivity vs temperature for each doping at V_{bias} = 10V. c) Change in normalized Hooge parameter (low frequency noise) for the WB at different temperatures for each concentration, and in d) signal amplitude, i.e. the height of the maxima in the voltage output for V_{bias} = 10V normalized by V_{bias}, which decreases with temperature until it gets too close to the T_C.*

Finally, to separate the effects of temperature and Sr content, we analysed the measured sensitivity and noise values for the same ratio of T/T_C for the four different concentrations displaying FM at 310 K, keeping this T/T_C ratio at approximately 0.93. In fact, considering that close to T_C , the magnetization follows a potential law $M(T) \propto \left(1 - \frac{T}{T_c}\right)^\beta$ (where β takes the value $1/2$, e.g. in the Stoner model or the Weiss model [26],[27]), we can assume that for the same ratio T/T_C for different x, the systems lie in the same relative position of the phase.

This assumption is validated by Figure 5a in which the sensitivity vs. doping at fixed T/T_C =0.93, is almost constant at 0.0445 %/mT. Figure 5b presents α_H/n vs. doping at the maximum T/T_C. It is clearly observed that it follows a Gaussian-like shape centred around x = 0.25, suggesting a correlation with the SOC strength.

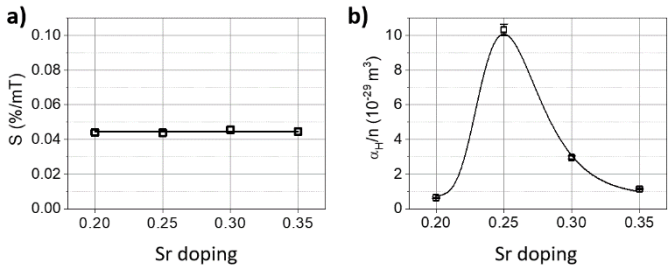

Figure 5. *a) Constant behavior of the sensitivity (0.0445 %/mT) when keeping the same ratio of T/T_C = 0.93 for all concentrations. b) Variation of the Hooge parameter versus Sr content for the maximum T/T_C ratio measured.*

To advance in the qualitative comprehension of the relation between SOC and α_H/n, we consider a model based on the DE mechanism [28],[29]. Accordingly, our system can be described by a Hamiltonian [28] that includes the hopping of the electrons between sites, the Coulomb repulsion that prevents double occupancy, a Hund term that accounts for the coupling between the t_{2g} spins and e_g spins, and JT term due to crystal distortion that breaks the degeneracy of the e_g orbitals. In manganites, the hopping of the itinerant electrons and the JT energy splitting are more relevant [29],[30],[31], with the latter increasing with x [17]. The hopping integral depends on the number of Mn^{4+} and Mn^{3+} ions and is expected to be symmetrical around x = 0.31 [21]. In contrast, JT comes into play due to the tensile strain that elongates the O-Mn-O bonds favoring the in-plane orbitals occupancy and orbital mixing, enhancing orbital angular momentum. While JT promotes the localization of the itinerant electrons by removing the energy degeneracy, the larger the hopping term the more delocalized are the electrons. Thus, the competition between these two effects determines the shift of the SOC towards lower Sr doping. On another hand, the electron mobility is found to be proportional to the effective exchange parameter, J_{eff} [32],[33]. Clearly J_{eff} depends on the competition between the two contributions, and since $1/f$ noise is related with the electron mobility and its fluctuations [34], α_H/n is expected to shift accordingly.

3. Conclusions

In conclusion, by resorting to a combination of experiments based on magneto-transport, X-ray magnetic dichroism and low frequency noise measurements, we have studied the properties of AMR ultra-low magnetic field sensors based on LSMO epitaxial film. We have determined the optimal Sr doping for the human body operation temperature and correlated the $1/f$ electronic noise measured in WB devices with SOC strength both maximized at x = 0.25 although the optimal FM ordering is at x = 0.30. Based on our experimental results, we argue that this difference is due to the competition between the electron hopping, hence electron mobility, and the JT distortions. Moreover, our low frequency noise experiments at T = 310 K, for 0.15 < x < 0.45 demonstrates that the sensitivity increases with x, while the normalized Hooge parameter is maximized at x = 0.25. Our temperature dependent experiments finally demonstrate that LSMO AMR with x = 0.35 at T = 310 K, i.e., temperature of human body, presents the best detection performance in terms of sensitivity and low noise, fulfilling the operational requirements for biomedical applications. Moreover, the electronic noise correlates with the optimal doping levels. This insight is critical for developing sensors with ultra-low detection limits.

Acknowledgements

This research was supported by MCIN/AEI, Spain/10.13039/501100011033 through Projects PID2021-122980OB-C52, CNS2022-136143, and PID2020-116181RB-C31, and by the Comunidad de Madrid through project TEC-2024/TEC-380 “Mag4TIC”. This work has been partially performed in the framework of the Nanoscience Foundry and Fine Analysis (NFFA-MUR Italy Progetti Internazionali) project (www.trieste.NFFA.eu). The XAS-XMCD experiments were performed at APE-HE beamline at Elettra synchrotron, Trieste through NFFA-Trieste proposal N.2019_003. RSL thanks Region Normandie for partial funding of the PhD grant through the RIN50 program.

References

[1] Zheng, C. *et al.*, “Magnetoresistive Sensor Development Roadmap (Non-Recording Applications),” *IEEE Trans. Magn.* **55**, 1–30 (2019). https://doi.org/10.1109/TMAG.2019.2896036

[2] Dieny, B. *et al.*, “Opportunities and challenges for spintronics in the microelectronics industry,” *Nat. Electron.* **3**, 446–459 (2020). https://doi.org/10.1038/s41928-020-0461-5

[3] Khan, M. A. *et al.*, “Magnetic sensors – A review and recent technologies,” *Eng. Res. Express* **3**, 022005 (2021). https://doi.org/10.1088/2631-8695/ac0838

[4] Campbell, I. A. *et al.*, “The spontaneous resistivity anisotropy in Ni-based alloys,” *J. Phys. C: Solid State Phys.* **3**, S95 (1970). https://doi.org/10.1088/0022-3719/3/1S/310

[5] McGuire, T., and Potter, R., “Anisotropic magnetoresistance in ferromagnetic 3d alloys,” *IEEE Trans. Magn.* **11**, 1018–1038 (1975). https://doi.org/10.1109/TMAG.1975.1058782

[6] Ziese, M., and Sena, S. P., “Anisotropic magnetoresistance of thin $La_{0.7}Ca_{0.3}MnO_3$ films,” *J. Phys.: Condens. Matter* **10**, 2727–2737 (1998). https://doi.org/10.1088/0953-8984/10/12/012

[7] Enger, L. G. *et al.*, “Key Parameters for Detectivity Improvement of Low Noise Anisotropic Magnetoresistive Sensors Made of $La_{2/3}Sr_{1/3}MnO_3$ Single Layers on Vicinal Substrates,” *ACS Appl. Electron. Mater.* **5**, 729–739 (2023). https://doi.org/10.1021/acsaelm.2c01096

[8] Vera, A. *et al.*, “High-Performance Implantable Sensors based on Anisotropic Magnetoresistive $La_{0.67}Sr_{0.33}MnO_3$ for Biomedical Applications,” *ACS Biomater. Sci. Eng.* **9**, 1020–1029 (2023). https://doi.org/10.1021/acsbiomaterials.2c01147

[9] Salamon, M. B., and Jaime, M., "The physics of manganites: Structure and transport," *Rev. Mod. Phys.* **73**, 583–628 (2001). https://doi.org/10.1103/RevModPhys.73.583

[10] Zener, C., "Interaction between the d-Shells in the Transition Metals. II. Ferromagnetic Compounds of Manganese with Perovskite Structure," *Phys. Rev.* **82**, 403–405 (1951). https://doi.org/10.1103/PhysRev.82.403

[11] Millis, A. J. *et al.*, "Quantifying strain dependence in 'colossal' magnetoresistance manganites," *J. Appl. Phys.* **83**, 1588–1591 (1998). https://doi.org/10.1063/1.367310

[12] Chaluvadi, S. K. *et al.*, "Epitaxial strain and thickness dependent structural, electrical and magnetic properties of $La_{0.67}Sr_{0.33}MnO_3$ films," *J. Phys. D: Appl. Phys.* **53**, 375005 (2020). https://doi.org/10.1088/1361-6463/ab8e7b

[13] Perna, P. *et al.*, "Tailoring magnetic anisotropy in epitaxial half-metallic $La_{0.7}Sr_{0.3}MnO_3$ thin films," *J. Appl. Phys.* **110**, 013919 (2011). https://doi.org/10.1063/1.3605542

[14] Perna, P. *et al.*, "Magnetization reversal in half-metallic $La_{0.7}Sr_{0.3}MnO_3$ films grown onto vicinal surfaces," *J. Appl. Phys.* **109**, 07B107 (2011). https://doi.org/10.1063/1.3560893

[15] Perna, P. *et al.*, "Imaging the magnetization reversal of step-induced uniaxial magnetic anisotropy in vicinal epitaxial $La_{0.7}Sr_{0.3}MnO_3$ films," *New J. Phys.* **12**, 103033 (2010). https://doi.org/10.1088/1367-2630/12/10/103033

[16] Perna, P. *et al.*, "Engineering Large Anisotropic Magnetoresistance in $La_{0.7}Sr_{0.3}MnO_3$ Films at Room Temperature," *Adv. Funct. Mater.* **27**, 1700664 (2017). https://doi.org/10.1002/adfm.201700664

[17] Chaluvadi, S. *et al.*, "Electronic Properties of Fully Strained $La_{1-x}Sr_xMnO_3$ Thin Films Grown by Molecular Beam Epitaxy ($0.15 \leq x \leq 0.45$)," *ACS Omega* **7**, 14571–14578 (2022). https://doi.org/10.1021/acsomega.1c06529

[18] Jiménez, E. *et al.*, "Vectorial Kerr magnetometer for simultaneous and quantitative measurements of the in-plane magnetization components," *Rev. Sci. Instrum.* **85**, 053904 (2014). https://doi.org/10.1063/1.4871098

[19] van der Laan, G., and Figueroa, A. I., "X-ray magnetic circular dichroism: A versatile tool to study magnetism," *Coord. Chem. Rev.* **277–278**, 95–129 (2014). https://doi.org/10.1016/j.ccr.2014.03.018

[20] Koide, T. *et al.*, "Close correlation between the magnetic moments, lattice distortions, and hybridization in $LaMnO_3$ and $La_{1-x}Sr_xMnO_{3+\delta}$: Doping-dependent magnetic circular X-ray dichroism study," *Phys. Rev. Lett.* **87**, 246404 (2001). https://doi.org/10.1103/PhysRevLett.87.246404

[21] Goodenough, J. B., "Theory of the role of covalence in the perovskite-type manganites [La, M (II)] MnO_3," *Phys. Rev.* **100**, 564 (1955). https://doi.org/10.1103/PhysRev.100.564

[22] Thole, B. T., and van der Laan, G., "Linear relation between x-ray absorption branching ratio and valence-band spin-orbit expectation value," *Phys. Rev. A* **38**, 1943 (1988). https://doi.org/10.1103/PhysRevA.38.1943

[23] Sim, J.-H., Yoon, H., Park, S. H., and Han, M. J., "Calculating branching ratio and spin-orbit coupling from first principles: A formalism and its application to iridates," *Phys. Rev. B* **94**, 115149 (2016). https://doi.org/10.1103/PhysRevB.94.115149

[24] Perna, P. *et al.*, "Direct experimental determination of the anisotropic magnetoresistive effects," *Appl. Phys. Lett.* **104**, 202407 (2014). https://doi.org/10.1063/1.4878555

[25] Hooge, F. N., "1/f noise is no surface effect," *Phys. Lett. A* **29**, 139–140 (1969). https://doi.org/10.1016/0375-9601(69)90076-0

[26] Chikazumi, Sōshin, and Graham, C. D., Jr., *Physics of Ferromagnetism* (Oxford University Press, 1997; online edn., Oxford Academic, 2023). https://doi.org/10.1093/oso/9780198517764.001.0001

[27] Mohn, P., "Landau theory for the Stoner model," in *Magnetism in the Solid State: An Introduction*, Vol. 134, Springer-Verlag, Berlin (2003), pp. 139–145. https://doi.org/10.1007/3-540-30981-0

[28] Coey, J. M. D., Viret, M., and von Molnár, S., "Mixed-valence manganites," *Adv. Phys.* **48**, 167–293 (1999). https://doi.org/10.1080/000187399243455

[29] Weiße, A., Loos, J., and Fehske, H., "Considerations on the quantum double-exchange Hamiltonian," *Phys. Rev. B* **64**, 054406 (2001). https://doi.org/10.1103/PhysRevB.64.054406

[30] Izyumov, Y. A., and Skryabin, Yu. N., "Double exchange model and the unique properties of the manganites," *Phys. Usp.* **44**, 109–134 (2001). https://doi.org/10.1070/PU2001v044n02ABEH000840.

[31] Opel, M., "Spintronic oxides grown by laser-MBE," *J. Phys. D: Appl. Phys.* **45**, 033001 (2012). https://doi.org/10.1088/0022-3727/45/3/033001

[32] Stancil, D. D., and Prabhakar, A., *Spin Waves: Theory and Applications* (Springer, 2009). https://doi.org/10.1007/978-0-387-77865-5

[33] Kittel, C., *Introduction to Solid State Physics*, 8th edn. (John Wiley & Sons, New York, NY, 2004). ISBN 978-0-471-41526-8

[34] Kogan, Sh., *Electronic Noise and Fluctuations in Solids* (Cambridge University Press, Cambridge, 1996). https://doi.org/10.1017/CBO9780511551666

SUPPLEMENTARY INFORMATION

Low-Noise Anisotropic Magnetoresistance Sensing at 310 K: Unveiling the Optimal Doping Window in $La_{1-x}Sr_xMnO_3$ Films

Raul Solis Leon[1,2,3], Ines Garcia Manuz[2,3], Sandeep Kumar Chaluvadi[4], Victor Pierron[1], Vincent Polewczyk[4], Aleksandr Yu Petrov[4], Giovanni Vinai[4], Alain Pautrat[5], Fernando Ajejas[3], Bruno Guillet[1], Stéphane Flament[1], Pasquale Orgiani[4], Paolo Perna[3,*], Laurence Mechin[1,*]

[1] Université Caen Normandie, ENSICAEN, CNRS, Normandie Univ., GREYC UMR6072, F,14050 Caen CEDEX, France
[2] Departamento de Física de la Materia Condensada & Condensed Matter Physics Center (IFIMAC), Universidad Autónoma de Madrid, Campus de Cantoblanco, Madrid 28049, Spain
[3] IMDEA Nanoscience, C/ Faraday 9, Campus de Cantoblanco, Madrid 28049, Spain
[4] CNR - Istituto Officina dei Materiali (IOM), S.S. 14 km 163.5, I-34149, Trieste, Italy
[5] Université Caen Normandie, ENSICAEN, CNRS, Normandie Univ., CRISMAT UMR6508, 14050 Caen CEDEX, France

E-mail: paolo.perna@imdea.org ; laurence.mechin@ensicaen.fr

A1. Magneto-Optical Kerr effect magnetometry

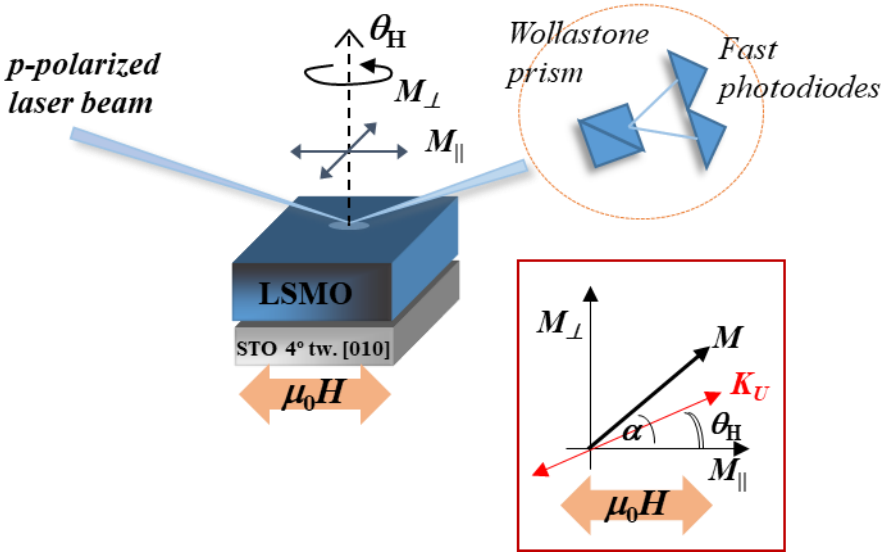

Figure S1. Schematic representation of the LSMO film grown onto STO(001) substrate with miscut angle δº = 4º (from the [001] towards [010] crystallographic direction) and of the vectorial-Kerr configuration. The two-fold symmetry of the substrate surface determines a defined two-fold (uniaxial) magnetic anisotropy with anisotropy constant K_U. The magnetization easy-axis (e.a.) is parallel to the [100] direction, whereas the hard-axis (h.a.) results perpendicular to it, i.e. [010]. In the side-box the illustration of the measurements configuration is sketched for clarity. It defines the angles between the magnetic field and the anisotropy direction $\boldsymbol{\theta_H} \equiv (\widehat{\boldsymbol{H},\boldsymbol{K_U}})$, the magnetic field and the magnetization of the system $\boldsymbol{\alpha} \equiv (\widehat{\boldsymbol{M},\boldsymbol{H}})$ (i.e., magnetic torque). Note that in our measurements, the magnetic field is kept fixed and the sample is rotated. The two orthogonal in-plane magnetization components are parallel ($M_{\parallel}$) and perpendicular ($M_{\perp}$) to the magnetic field ***H***.

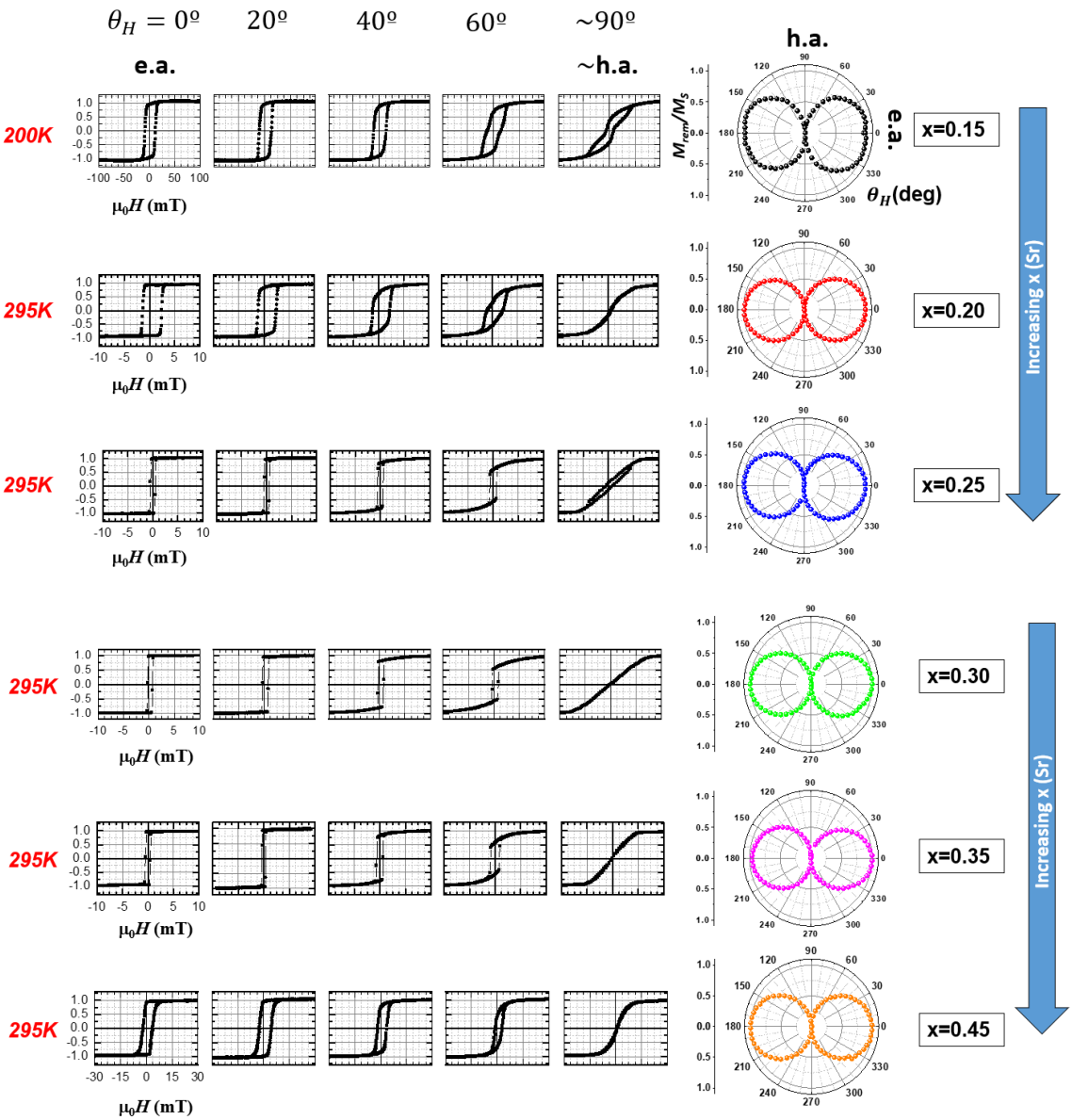

Figure S2. Results from Magneto-optical Kerr Effect measurements (MOKE) for the samples of concentrations ranging from x=0.15 to x=0.45. For x=0.15, measurements at 200K are reported since Curie temperature is T=253K. For the other concentrations, the measurements were conducted at T=295K. In the left part of the figure the hysteresis cycles are displayed at different orientations with respect to the easy axis (i.e., $\theta_H = \left(\widehat{H, K_u}\right)$, with H being the applied magnetic field and K_u the direction of the magnetization e.a.). The black curve represent the magnetization component parallel to the applied magnetic field and exhibits a square shape at the easy axis direction and almost a fully reversible behavior when the field is applied at approx. 90º. These are the typical features of a defined uniaxial magnetic anisotropy, as also evinceed, for all the concentrations investigated, by the angular evolution of the magnetization remanence normalised to the saturation magnetization (right part of the figure), which presents the typical 2-fold symmetry, with no remanence at θ_H =90º and 270º and its maximum value at 0º and 180º.

A2. X-ray absorption and magnetic circular dichroism (XAS-XMCD) experiments

X-ray absorption and magnetic circular dichroism spectra (XAS-XMCD) using circular polarized light with opposite helicities were performed at the APE-HE beamline at Elettra synchrotron, Trieste.

From the spectra, integrated sum and difference, we extrated the spin and orbital magnetic moments[1]:

$$m_S(\mu_B) = -\frac{n_h}{P\cos\theta}\cdot\frac{6p-4q}{3r} \quad (1)$$

$$m_L(\mu_B) = -\frac{n_h}{P\cos\theta}\cdot\frac{4q}{3r} \quad (2)$$

Where $n_h = 10 - n_{3d}$ is the number of holes and $n_{3d}(x) = (4+\Delta n_{3d})\cdot(1-x) + (3+\Delta n'_{3d})\cdot x$ is interpolated from the calculated charge transfers [2], $\Delta n_{3d} = 0.5$ for $LaMnO_3$ and $\Delta n'_{3d} = 0.8$ for $SrMnO_3$.

On another hand, the ratio of the total line strength of the L_2 and L_3 edges in XAS is related to the expectation value of the spin-orbit coupling (SOC) operator. It is a measure of the valence-band SO interactions. The branching ratio measures the angular part of the SOC operator[3]:

$$\frac{I_j}{I_2+I_3} = \frac{2j+1}{2(2l_c+1)} \pm A(l_c, l_v, n_h)\,\langle \boldsymbol{L}\cdot\boldsymbol{S}\rangle \quad (3)$$

Applying (3) to our case and extracting the expectation SOC value we get:

$$\langle \boldsymbol{L}\cdot\boldsymbol{S}\rangle = n_h\,\frac{2-{I_2}/{I_3}}{1+{I_2}/{I_3}} \quad (4)$$

The integral of the absorption, r, must be calculated after removing other transitions into higher unoccupied states or the continuum, by substracting an energy dependent step function such as $f(E) = h * \left[1-\frac{2}{3}\left(1+e^{\frac{E-E_1}{\varepsilon}}\right)-\frac{1}{3}\left(1+e^{\frac{E-E_2}{\varepsilon}}\right)\right]$.

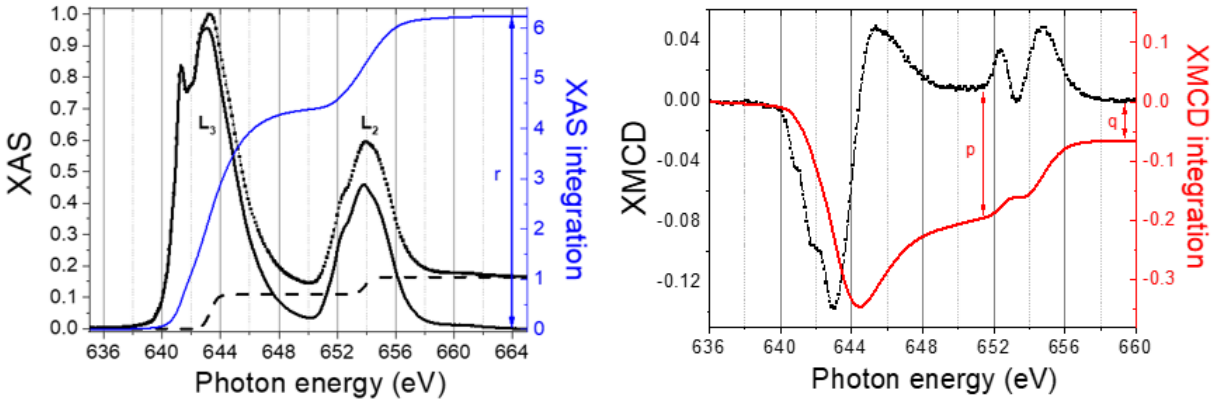

Figure S3. Schematics of how the parameters p, q, and r, required for the sum rule analysis, are obtained from the XAS and XMCD spectra of the L_2 and L_3 peaks. The left subfigure represents the XAS spectrum; The dashed black line represents the data without removing the background (dashed red line), while the solid black line corresponds to the spectrum after the removal. Finally, the blue line is obtained by integrating the spectrum without background. In a similar way, the right subfigure shows in black the difference of the total electron yield (TEY) for the different helicities, and the red line the integration of this curve.

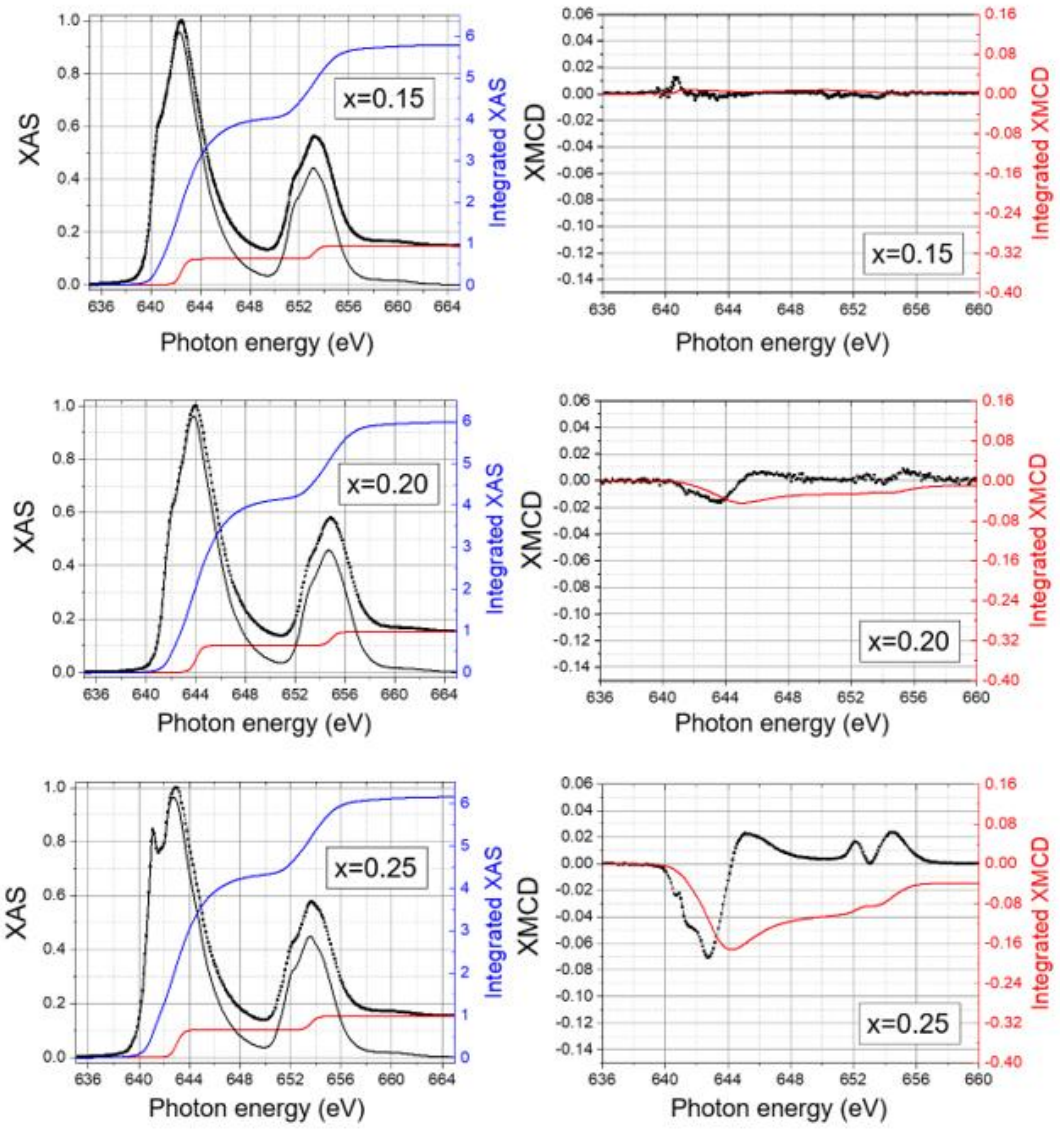

Figure S4. XAS and XMCD spectra for the sample x=0.15, 0.20, 0.25 at T = 295 K. The black pointed lines represent the experimental data for the sum and substraction of the total electron yield (TEY) for opposite helicities, respectively for the left and right subfigures. The blue curve on the XAS spectrum refers to the integrated curve and gives us the r parameter as the height of the second plateau. The red right curve represents the integrated curve for the XMCD signal, and allow us to obtain the p and q parameters as the height of the plateaus achieved after the L3 and L2 regions respectively.

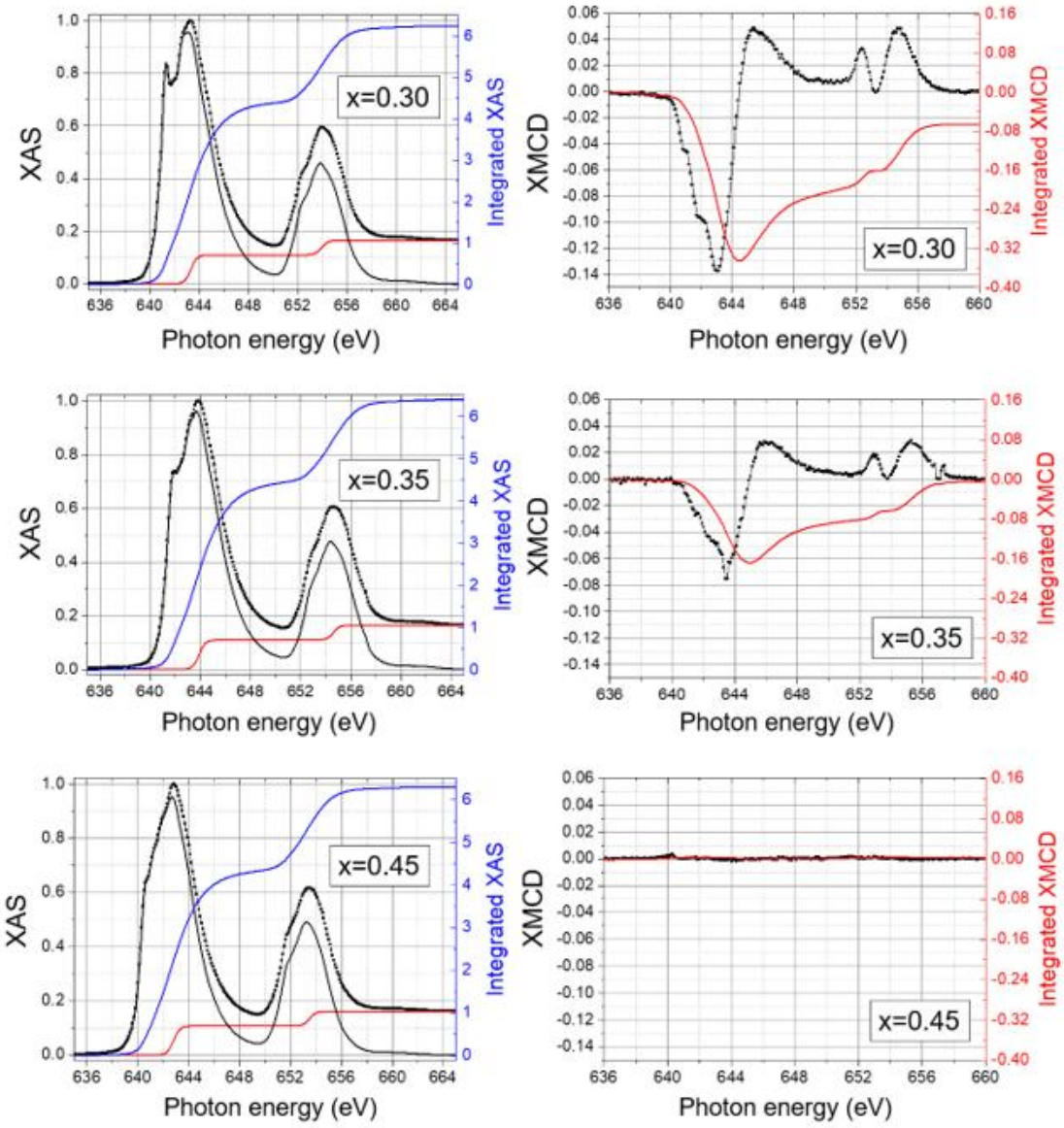

Figure S5. XAS and XMCD spectra for the sample x=0.30, 0.35, 0.45 at T=295K. The black pointed lines represent the experimental data for the sum and substraction of the total electron yield (TEY) for opposite helicities, respectively for the left and right subfigures. The blue curve on the XAS spectrum refers to the integrated curve and gives us the r parameter as the height of the second plateau. The red right curve represents the integrated curve for the XMCD signal, and allow us to obtain the p and q parameters as the height of the plateaus achieved after the L3 and L2 regions respectively.

Sr doping	n_h	p	q	r	$m_L(\mu_B)$	$m_S(\mu_B)$	$M_T(\mu_B)$
0.15	5.61	0.000	0.000	5.783	0.000	0.000	0.000
0.20	5.64	-0.026	-0.010	5.982	0.013	0.036	0.049
0.25	5.68	-0.101	-0.039	6.152	0.048	0.139	0.186
0.30	5.71	-0.197	-0.067	6.240	0.081	0.280	0.361
0.35	5.75	-0.082	-0.005	6.407	0.006	0.141	0.147
0.45	5.82	0.000	0.000	6.298	0.000	0.000	0.000

Figure S6. This table summarizes all the calculated integral parameters obtained from the XAS/XMCD spectra for each sample. We include the estimated spin, orbital and total magnetic moments from the sum rules previously shown.

A3. Device microfabrication

We have fabricated devices in Wheatstone Bridge (WB) geometry by a microlithography process. We deposited about 100 nm thick gold layers via ion beam deposition over the as-grown LSMO films. After deposition, we used the spin coating procedure to extend a uniform thin layer of photoresist (Shipley S1813), to subsequently introduce it in the UV laser lithography system (DMO MicroWriter). This is to selectively expose the resin to design the contact pads. Posteriorly, we immersed the sample into a developer solution (Microposit Developer) and after, into a KI solution that etches the undesired gold. The second step of the procedure is conducted to pattern the WB structures. It starts with the utilization of spin coating to extend once more a thin layer of resist and expose it afterwards, so as to fix the resin (developing stage). The following step is to introduced the samples in vacuum to perform Ion Beam Etching in Ar, to remove the unprotected LSMO. Finally, it is critical to remove the resin leftovers, so they are submerged in acetone.

A4. Electrical characterization of sensors

The nominal resistance of the Wheatstone bridges may be calculated by substracting the total noise power spectral density of the background (V_{bias}=0V) and the intrinsic noise of the amplifiers:

$$R = \sqrt{\left(\frac{2k_BT}{{i_{nA}}^2}\right)^2 + \frac{{S_v}^2{}_{input} - {e_{nA}}^2}{{i_{nA}}^2}} - \frac{2k_BT}{{i_{nA}}^2} \quad (5)$$

$$\Delta R = \sqrt{\frac{\left(\frac{{S_{vi}}^2}{{i_{nA}}^2}\frac{\Delta S_{vi}}{S_{vi}}\right)^2 + \left(\frac{{e_{nA}}^2}{{i_{nA}}^2}\frac{\Delta e_{nA}}{e_{nA}}\right)^2 + \left(R^2\frac{\Delta i_{nA}}{i_{nA}}\right)^2}{\left(R + \frac{2k_BT}{{i_{nA}}^2}\right)^2}} \quad (6)$$

Where (6) was calculated by the archetypical error propagation method.

	T/Tc (%)			
T(K) \ x(Sr)	**0.20**	**0.25**	**0.30**	**0.35**
292	92.70	86.65	82.95	82.72
300		89.02	85.23	84.99
310		91.99	88.07	87.82
320		94.96		
330			93.75	93.48

Figure S7. In this table we summarize the different temperatures at which we have perform AMR and noise measurements.

As we did not have T/Tc≈ 0.93 for the sample x=0.25, we fitted the sensitivity for the values that we have and checked that it follows a reasonably well linear trend. In any case, we could perform polynomial interpolation and the result would not be too far appart from the one obtained.

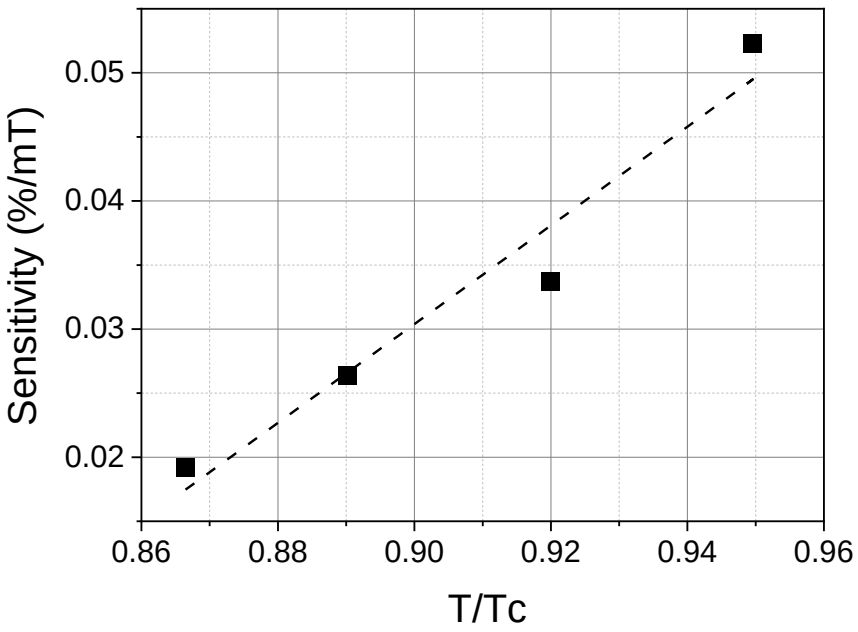

Figure S8. The picture displays the sensitivity values at different T/Tc ratios for the sample x=0.25 and its linear fitting.

For the noise, we cannot extract a tendency for a certain T/Tc in the same way as the sensitivty. Instead, we show the behavior of the Hooge parameter for the highest T/Tc for each sample, that do not deviate largely from each other.

A5. Low noise characterization

For the noise characterization we used amplifiers specifically designed so that its noise is negligible compared to the WB.

We could choose to fit either the power spectral density (S_v) or the detectivity (D), but the latter has higher error. This is due to the detectivity having two sources of errors both of experimental character, one coming from the extraction of the sensitivity (S) and the other because of the own noise measurement.

$$S_v = \sqrt{\frac{\alpha_H}{n}\frac{{V_{bias}}^2}{4\Omega f} + 4k_B RT + {e_n}^2} \tag{7}$$

$$D = \frac{1}{S}\sqrt{\frac{\alpha_H}{n}\frac{1}{4\Omega f} + \frac{4k_B R_0 T}{{V_{bias}}^2} + \frac{{e_n}^2}{{V_{bias}}^2}} \tag{8}$$

Where ${e_n}^2 = {e_{nA}}^2 + {R_0}^2\,{i_{nA}}^2$ is the amplifier noise. It comprehends two contributions, one that is independent of the input load resistance, e_{nA}, which is always sensed and amplified and i_{nA}, that generates a voltage noise when circulating throuhg a load resistance.

As aforementioned in the main article, there are three relevant noise contributions, the 1/f noise, the white noise (thermal) and the additional noise coming from the amplifiers. However, (8) shows that, if V_{bias} is large enough, the only remaining, non-negligible, term is the first one, which does not depend on V_{bias}.

In the case of the detectivity curves, as the voltage increases, the 1/f noise becomes the dominant term, thereby causing the curves to overlap in the low frequency region. On the other hand, the power spectral density curves are expected (and observed) to increase, especially in the low frequency region, with voltage.

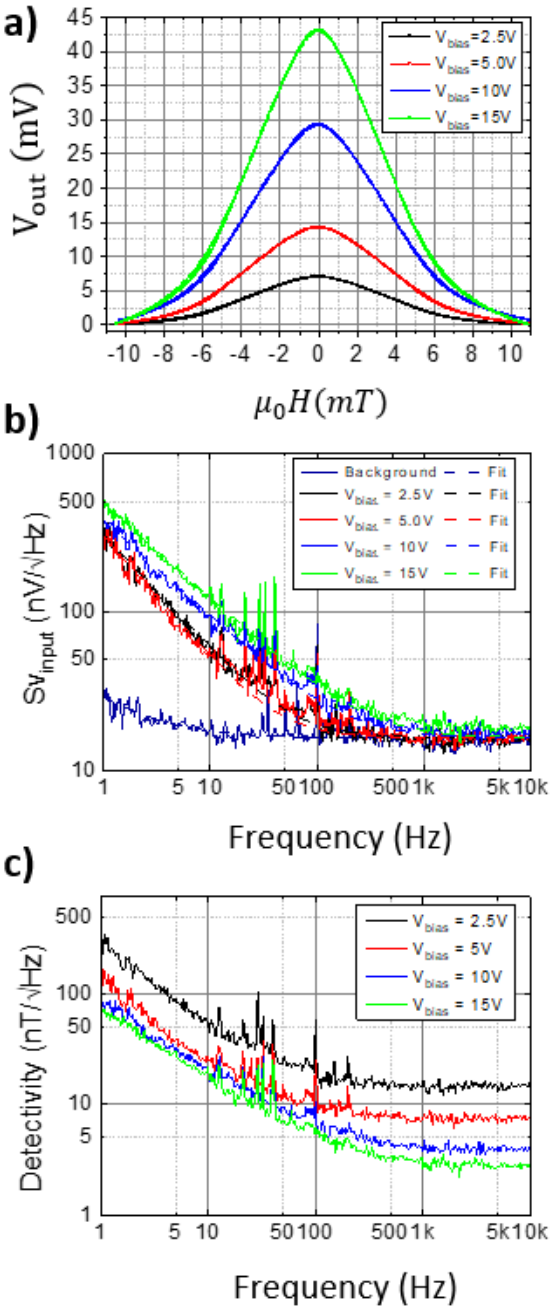

Figure S9. This figure corresponds to the sample x=0.20. Voltage value and voltage spectral density correspond to the value produced at the WB sensors level, before any amplification at T=292K. Panel a) exhibits the MR behavior for different values of V_{bias}. Panel b) displays the Power Spectral Density (PSD). Panel c) shows the detectivity curves obtained by dividing the PSD by the sensitivity calculated from the linear region of panel a) curves around $H_a/2$ at 292K. They also correspond to the maximum T/Tc ratio measured for this sample.

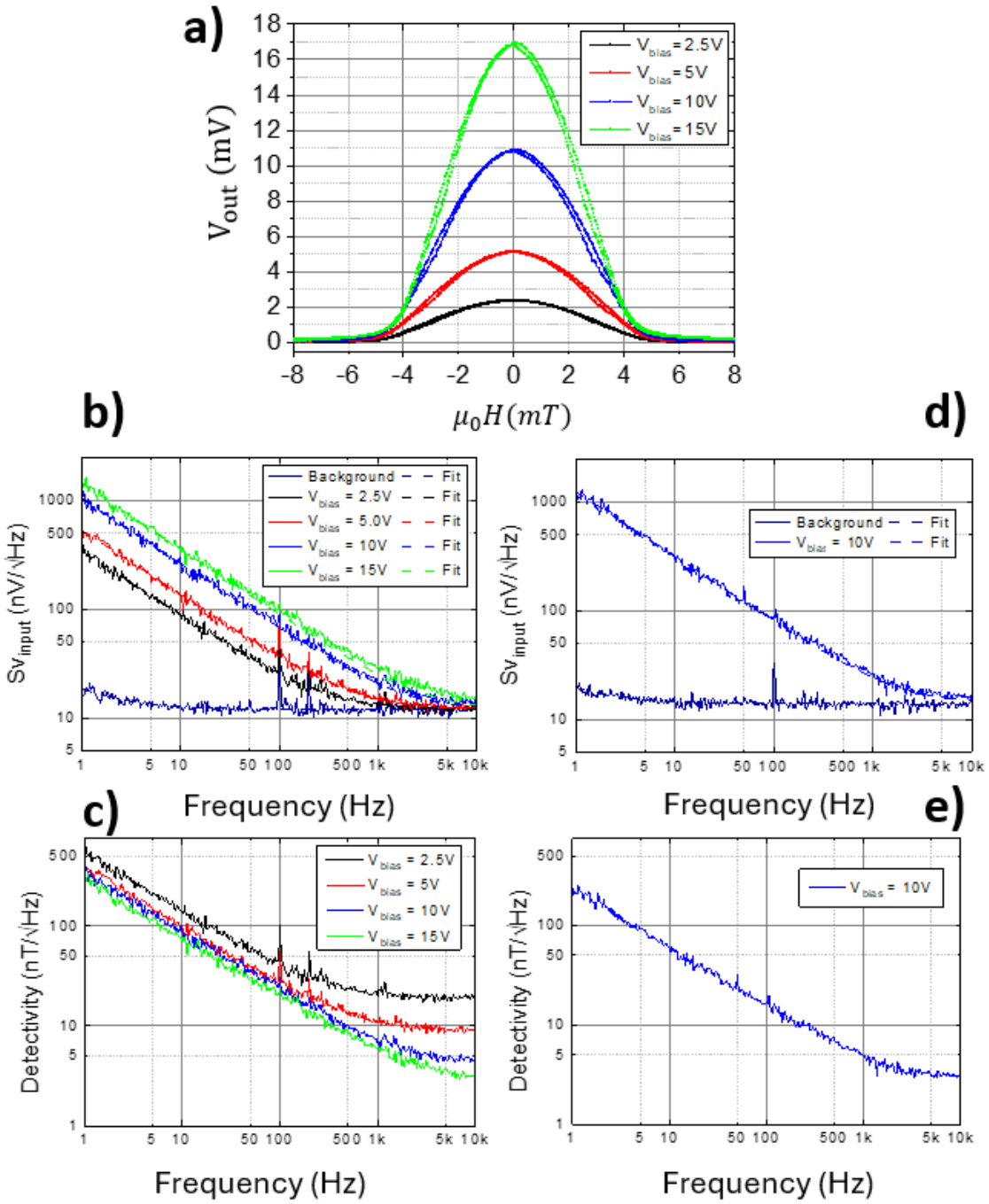

Figure S10. This figure corresponds to the sample x=0.25. Voltage value and voltage spectral density correspond to the value produced at the WB sensors level, before any amplification. Panel a) exhibits the MR behavior for different values of V_{bias} at T=310K. Panel b) displays the Power Spectral Density (PSD) at T=310K. Panel c) shows the detectivity curves obtained by dividing the PSD by the sensitivity calculated from the linear region of panel a) curves around $H_a/2$ at 310K. Panels d) and e) represent the same as b) and c) respectively but at T=320K, which corresponds to the maximum T/Tc ratio measured for this sample. Due to time limitations, we only conducted noise measurements at V_{bias}=10V for this temperature, as this is the bias voltage that we used througout the article to compare among samples.

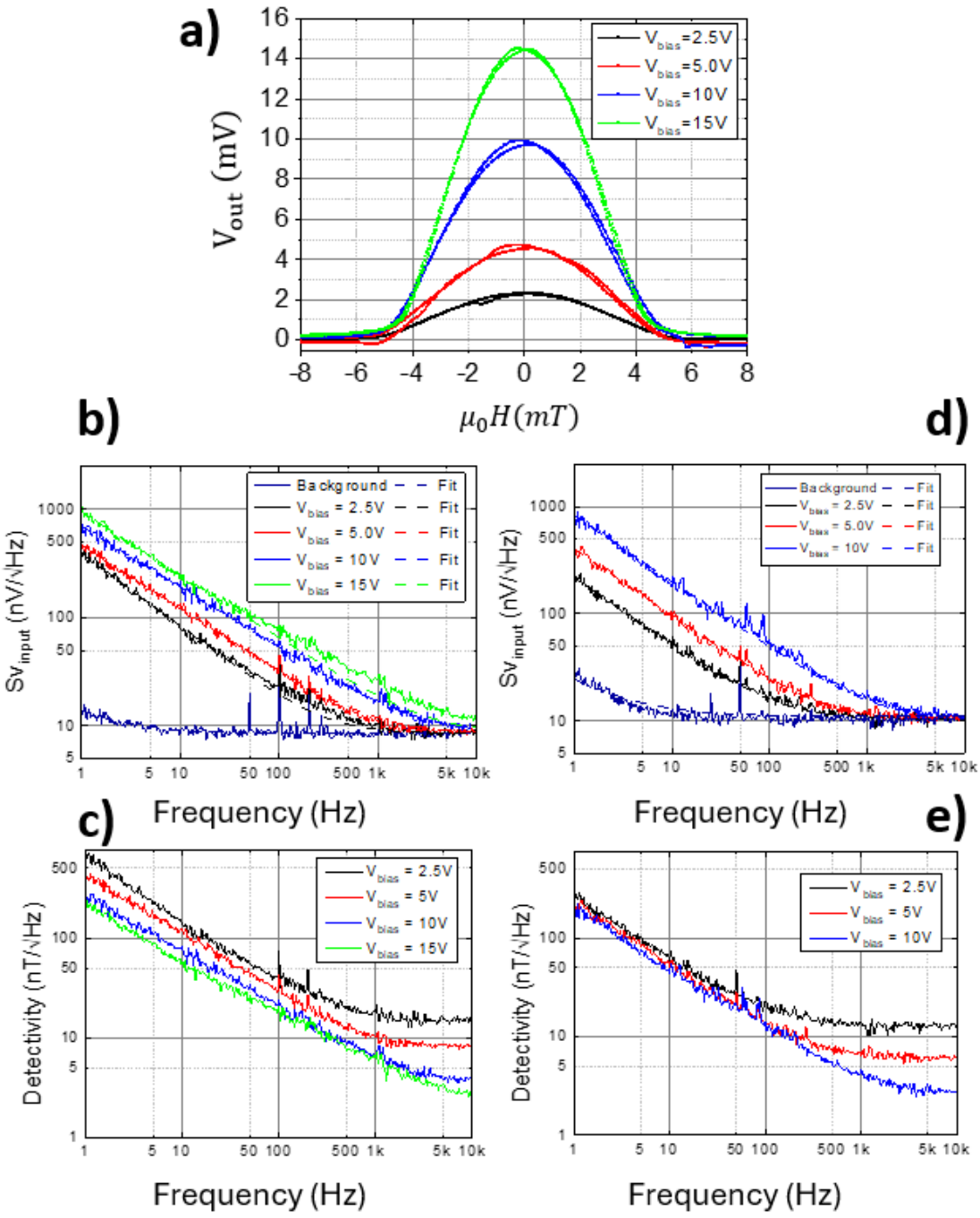

Figure S11. This figure corresponds to the sample x=0.30. Voltage value and voltage spectral density correspond to the value produced at the WB sensors level, before any amplification. Panel a) exhibits the MR behavior for different values of V_{bias} at T=310K. Panel b) displays the Power Spectral Density (PSD) at T=310K. Panel c) shows the detectivity curves obtained by dividing the PSD by the sensitivity calculated from the linear region of panel a) curves around $H_a/2$ at 310K. Panels d) and e) represent the same as b) and c) respectively but at T=330K, which corresponds to the maximum T/Tc ratio measured for this sample. The missing V_{bias}=15V curves at this temperature were removed due to them being distorted probably as a consequence of local heating that shift the effective temperature too close to the transition FM/PM.

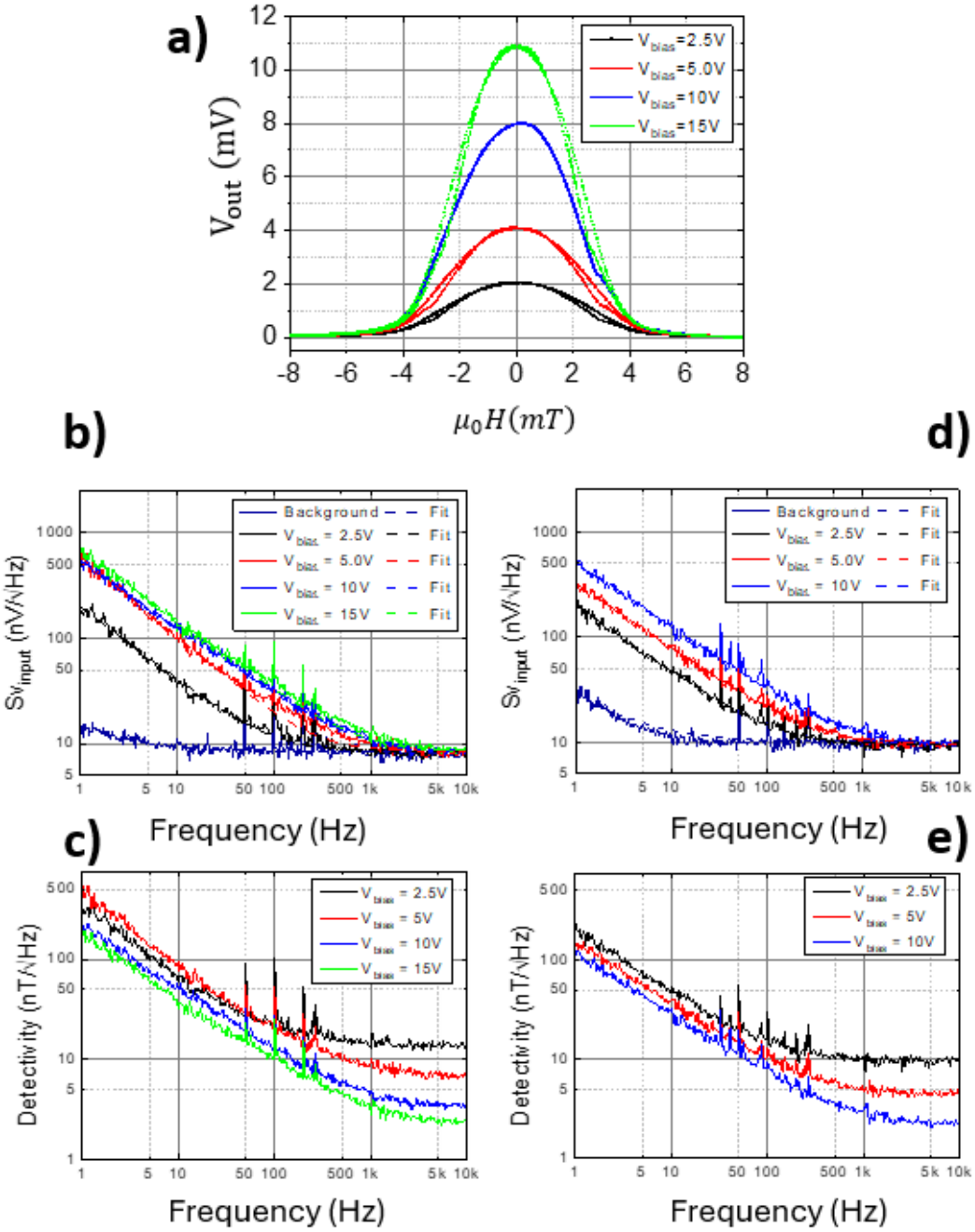

Figure S12. This figure corresponds to the sample x=0.35. Voltage value and voltage spectral densities correspond to the value produced at the WB sensors level, before any amplification. Panel a) exhibits the MR behavior for different values of V_{bias} at T=310K. Panel b) displays the Power Spectral Density (PSD) at T=310K. Panel c) shows the detectivity curves obtained by dividing the PSD by the sensitivity calculated from the linear region of panel a) curves around $H_a/2$ at 310K. Panels d) and e) represent the same as b) and c) respectively but at T=330K, which corresponds to the maximum T/Tc ratio measured for this sample. The missing V_{bias}=15V curves at this temperature were removed due to them being distorted probably as a consequence of local heating that shift the effective temperature too close to the transition FM/PM.

REFERENCES

1. van der Laan, G., and Figueroa, A. I., "X-ray magnetic circular dichroism: A versatile tool to study magnetism," *Coord. Chem. Rev.* **277–278**, 95–129 (2014). https://doi.org/10.1016/j.ccr.2014.03.018

2. Koide, T. *et al.*, "Close correlation between the magnetic moments, lattice distortions, and hybridization in $LaMnO_3$ and $La_{1-x}Sr_xMnO_{3+}\delta$: Doping-dependent magnetic circular X-ray dichroism study," *Phys. Rev. Lett.* **87**, 246404 (2001). https://doi.org/10.1103/PhysRevLett.87.246404

3. Thole, B. T., and van der Laan, G., "Linear relation between x-ray absorption branching ratio and valence-band spin-orbit expectation value," *Phys. Rev. A* **38**, 1943 (1988). https://doi.org/10.1103/PhysRevA.38.1943